Electronic Supplementary Material (ESI) for Energy & Environmental Science.

High performance thermoelectric composite via scalable and low-cost ink processing

A. N. M. Tanvir[a], Md Omarsany Bappy[a], Minxiang Zeng[b], Wenjie Shang[a], Ke Wang[c], K. Song[a], Y. Liu[d], E. Isotta[e], Mercouri G. Kanatzidis[d], G. Jeffrey Snyder[e], Alexander W. Dowling[c], Tengfei Luo[a], Yanliang Zhang*[a]

[a] Department of Aerospace and Mechanical Engineering, University of Notre Dame, Notre Dame, IN, USA 46556

[b] Department of Chemical Engineering, Texas Tech University, Lubbock, TX, USA 79409

[c] Department of Chemical and Biomolecular Engineering, University of Notre Dame, Notre Dame, IN, USA 46556

[d] Department of Chemistry, Northwestern University, Evanston, IL, USA 60208

[e] Department of Materials Science and Engineering, Northwestern University, Evanston, IL, USA 60208

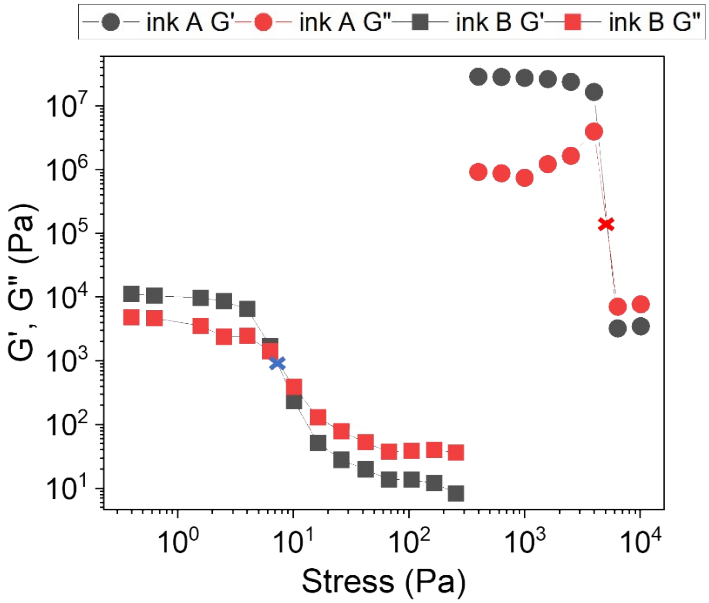

Fig. S1 Frequency sweep result of the ink was measured with Discover HR2 hybrid rheometer. Yield strength decreases to increase the printability of the ink. Ink A contains 16%wt of binder in the solvent, and ink B contains 33%wt binder in the solvent. G` and G" denote storage modulus and loss modulus of the ink, respectively. The blue and red cross denotes the yield strength (corresponding point at the x-axis) of the ink, which was decreased due to optimizing the binder concentration.

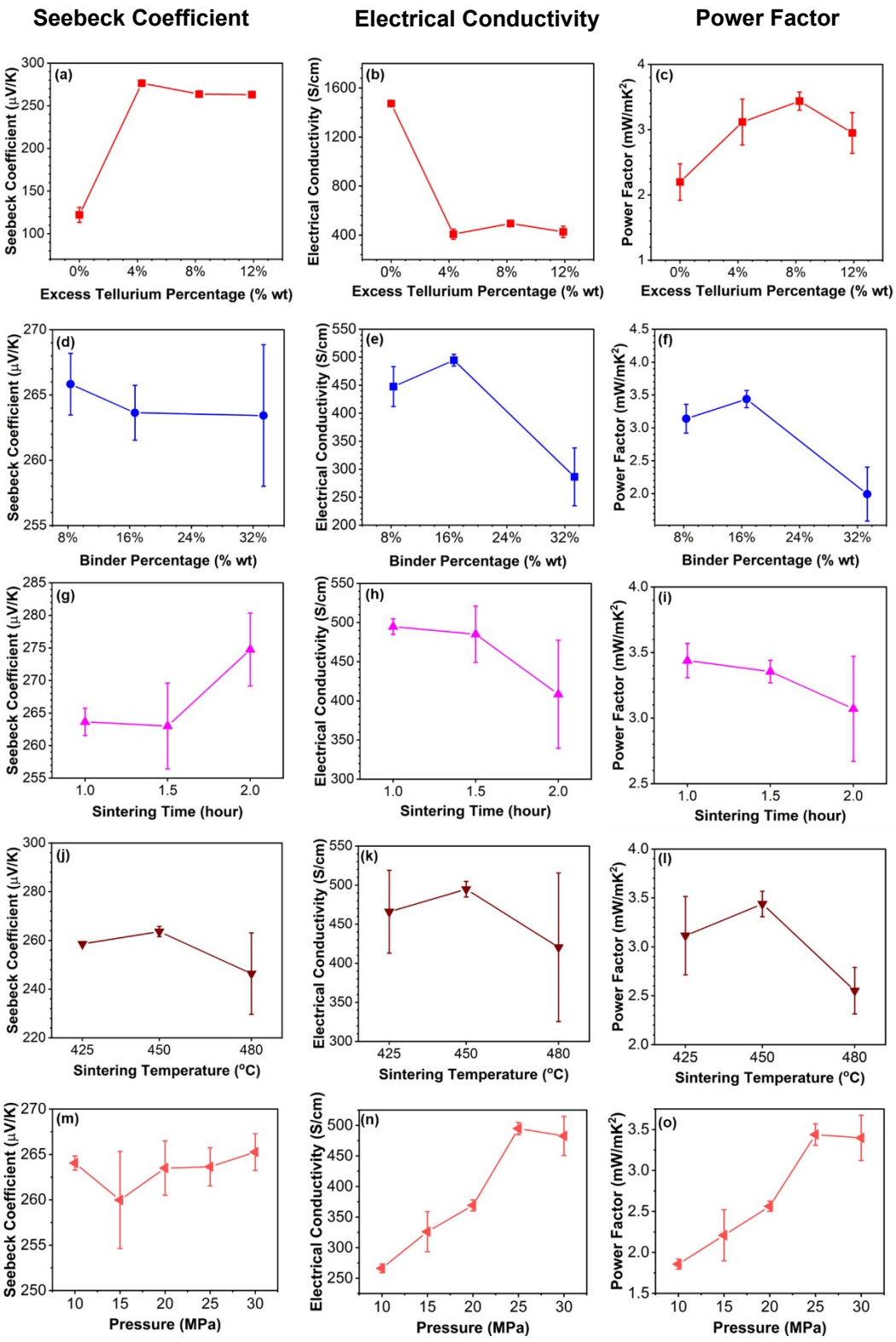

Fig. **S2** Optimization of different ink variables (a)-(c) Te amount, (d)-(f) binder concentration, (g)-(i) sintering time, (j)-(l) sintering temperature, (m) – (o) cold pressing pressure.

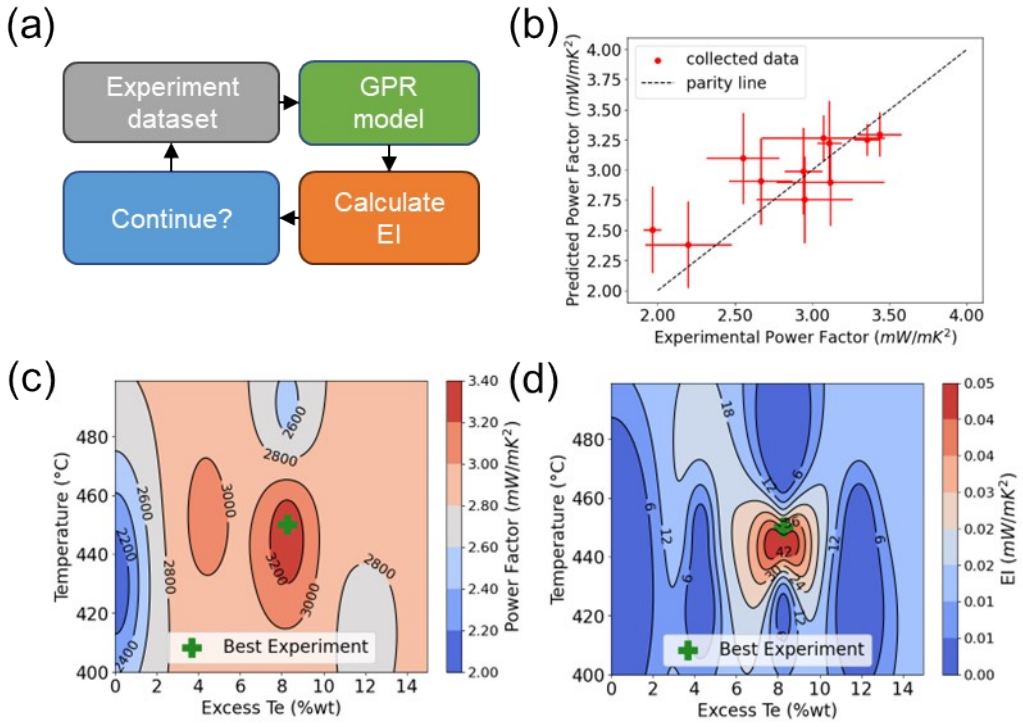

Fig. S3 (a) Bayesian optimization procedure. **Step 1**: The input variables include excess Te (x_1), temperature (x_2), sintering time (x_3), and binder concentration (x_4), denoted as $x \in R^4$; the output variable (objective) is power factor (y). **Step 2:** The Gaussian process regression (GPR) machine learning model, $f \sim GP(m(x),k(x,x))$, is trained based on the available data, where $m(x)$ is the mean function and $k(x,x)$ is the kernel function.[1] **Step 3**: The expected improvement (EI) acquisition function is calculated based on the prediction of GPR. Mathematically, $EI(x) = E\left[\max\left\{0,\mu_*(x) - f(x^+)\right\}\right]$, where $\mu_*(.)$ is the GPR prediction function and x^+ is the current maximal power factor experiment.[2] **Step 4**: The experiment with maximal EI value is recommended for the next round of experiments. For a full Bayesian optimization introduction, we refer to this comprehensive introduction.[3] (b) Leave-one-out parity plot for the dataset using a GPR model with predicted and experimental standard deviation (vertical and horizontal bars). The model combines the Matern 2.5 kernel and the white noise kernel. Predicted power factors are in close agreement with the ground truth values. (c) Heatmap of the GPR-predicted mean power factor as a function of excess Te and temperature. Sintering time is fixed at one hour, and binder concentration is fixed at 16%, where the optimal observed power factor is obtained. (d) Heatmap depicting the EI acquisition function, derived from the GPR-predicted mean and uncertainty of the power factor. The BO suggested optimal experimental condition (reddest circle) closely aligns with our best-performing completed experiment. The decision was made to halt further experiments with no obvious expected improvement (less than 90 μW/mK²).

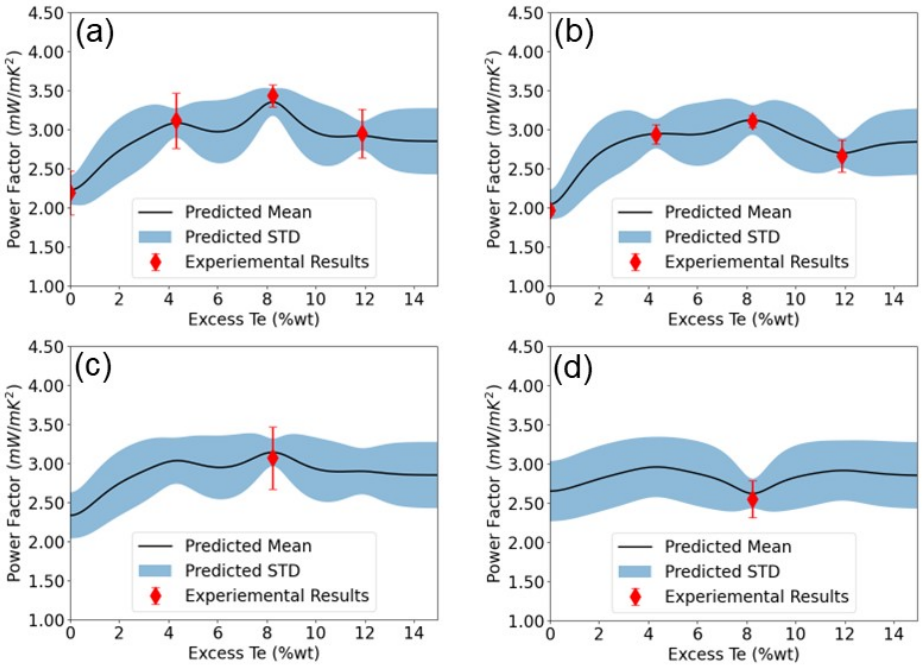

Fig. S4 One-dimensional sensitivity analysis of the power factor with respect to excess Te at different temperatures and sintering time conditions. The black line and blue region show GPR power factor prediction mean and uncertainty, respectively. The red diamonds and error bars show the experimentally measured power factor mean and standard deviation, respectively. (a) Temperature = 450 ºC, Time = 1h. (b) Temperature = 425 ºC, Time = 1h. (c) Temperature = 450 ºC , Time = 2h. (d) Temperature = 480 ºC, Time = 1h. These results show the highest power factor occurs around excess Te of 8 wt%, temperature of 450 ºC, and sintering time of one hour.

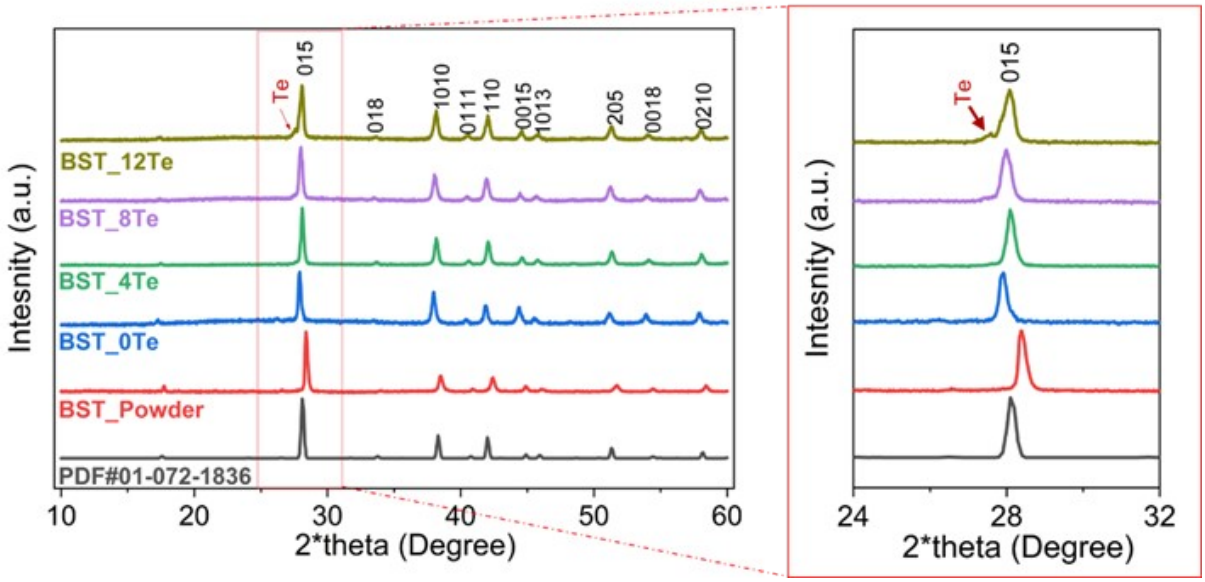

Fig. S5 X-ray diffraction result for BiSbTe pristine powder and sintered BiSbTe-Te sample after crushing into a powder again. The number before Te means the added extra Te. For example – BST_4Te means thermoelectric sample containing bismuth antimony telluride sample with added 4 %wt. Te. The highest power factor was found for the BST_8Te sample (BiSbTe-Te sample from the main text). The major peaks on all sintered powdered samples shifted to a lower angle compared to the pristine powder of BiSbTe. BST_0Te sample shifted to a much lower angle when compared to the samples with Te, which can be due to the larger crystallite size, microstrain, change in stoichiometry, as well as height difference between sample to sample.

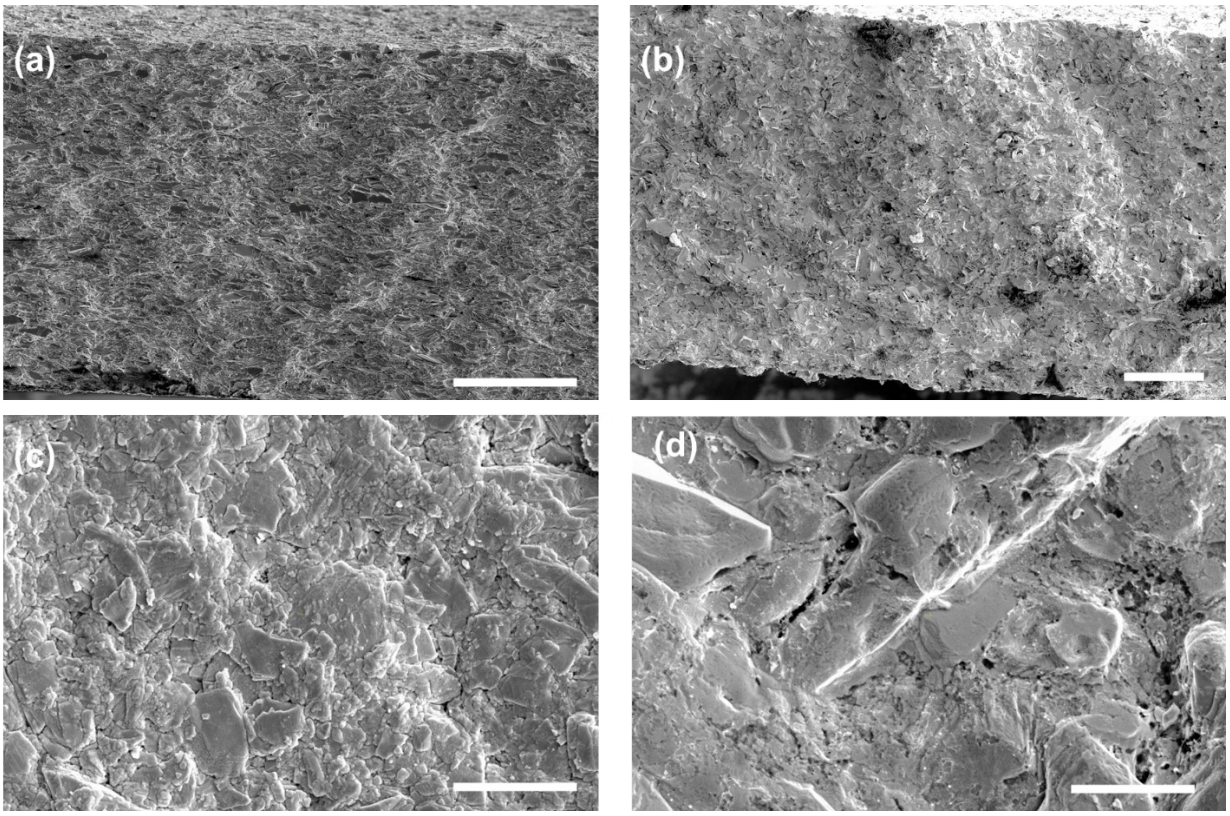

Fig. S6 Scanning electron microscopy images of the fractured cross-section of (a) BiSbTe, (b) BiSbTe-Te (both scale bar 5 μm) and the top plane of (c) cold pressed BiSbTe-Te showing porosities and disconnected powder particles compacted in a structure, (d) sintered BiSbTe-Te showing larger porosities (both scale bar 100 μm).

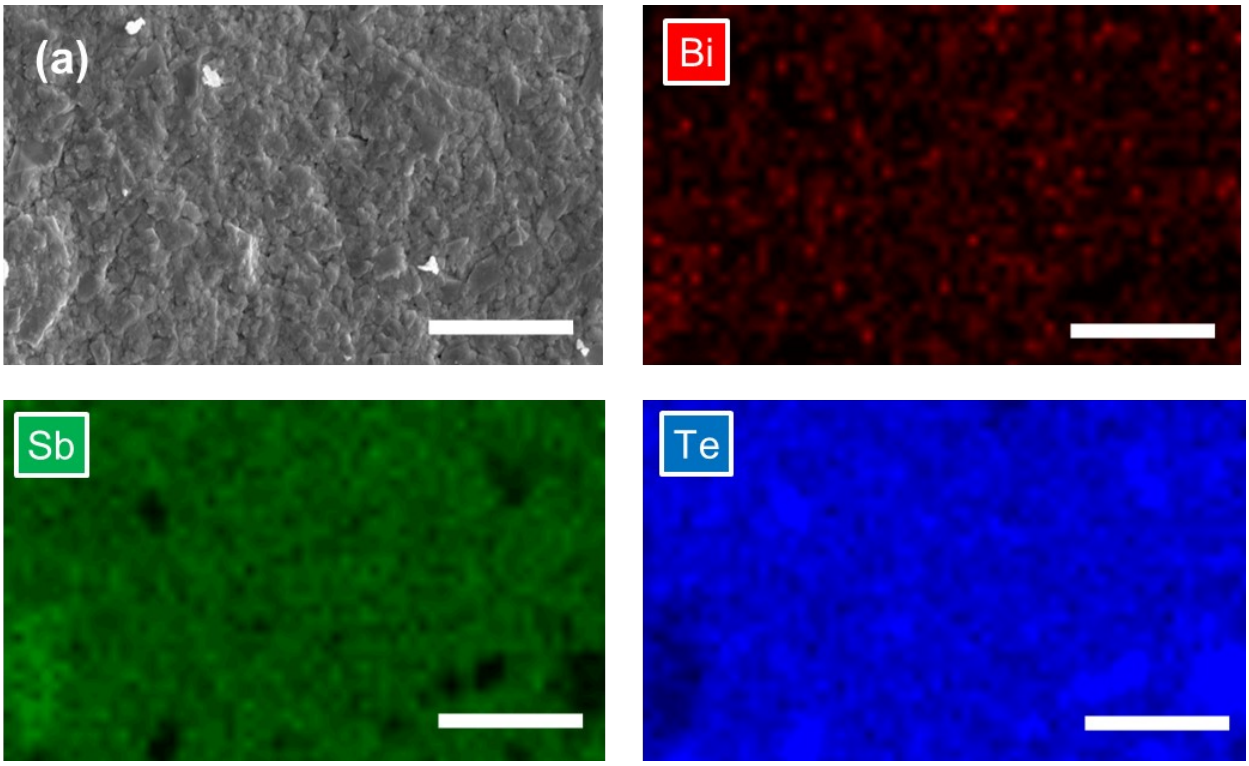

Fig. S7 Elemental mapping of cold pressed (before sintering) BiSbTe-Te from Top plane (plane perpendicular to pressing direction). Te is mainly concentrated at spots. scale bar 20 μm.

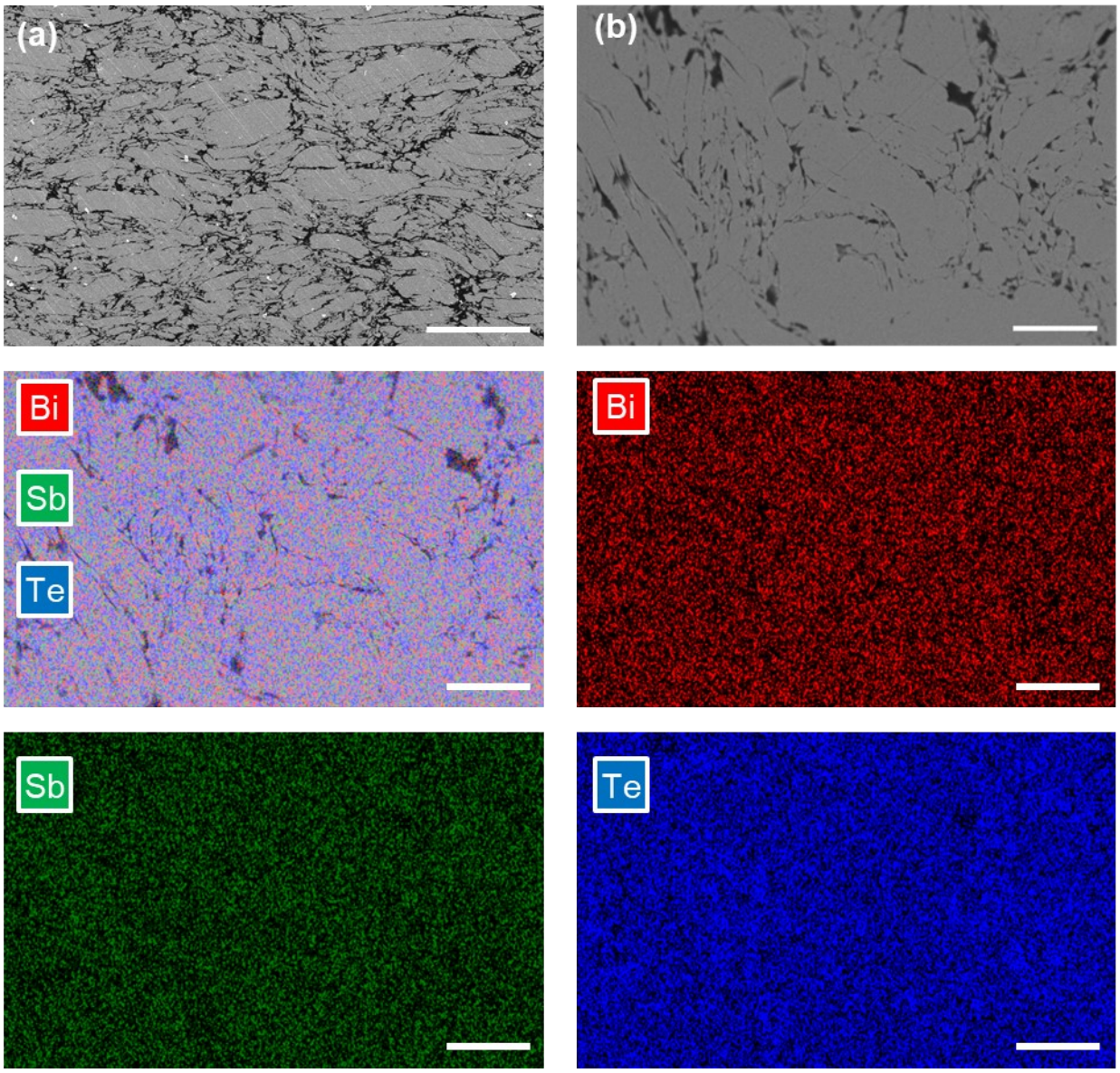

Fig. S8 (a) BiSbTe microstructure of the cross-section after polishing. Scale bar 5 μm. (b) SEM image of BiSbTe and its relevant EDS elemental map of showing uniform Te distribution over the microstructure. Scale bar 100 μm.

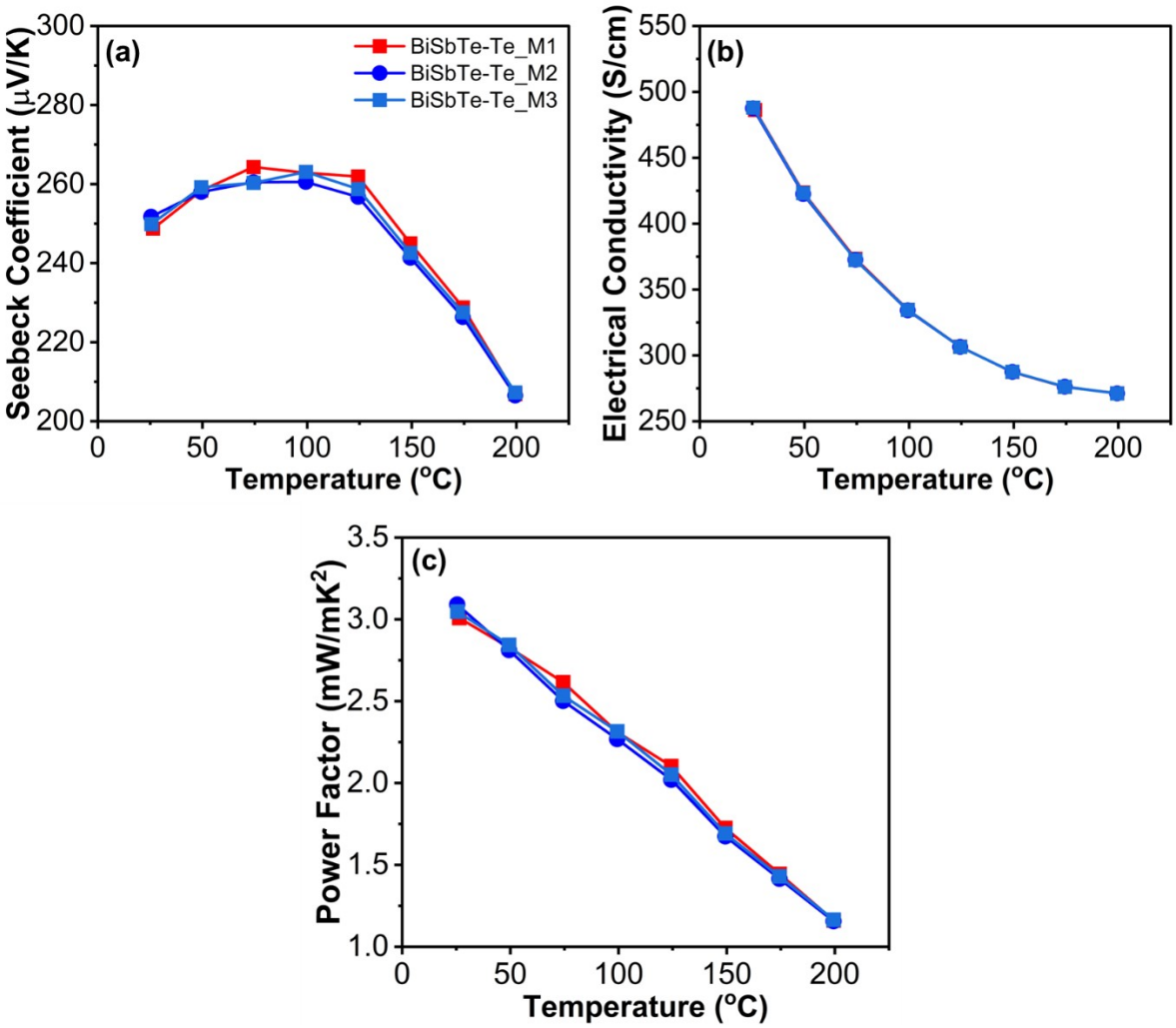

Fig. S9 BiSbTe-Te sample shows stable (a) Seebeck coefficient, (b) electrical conductivity and (c) power factor over consequent measurement showing stability over time.

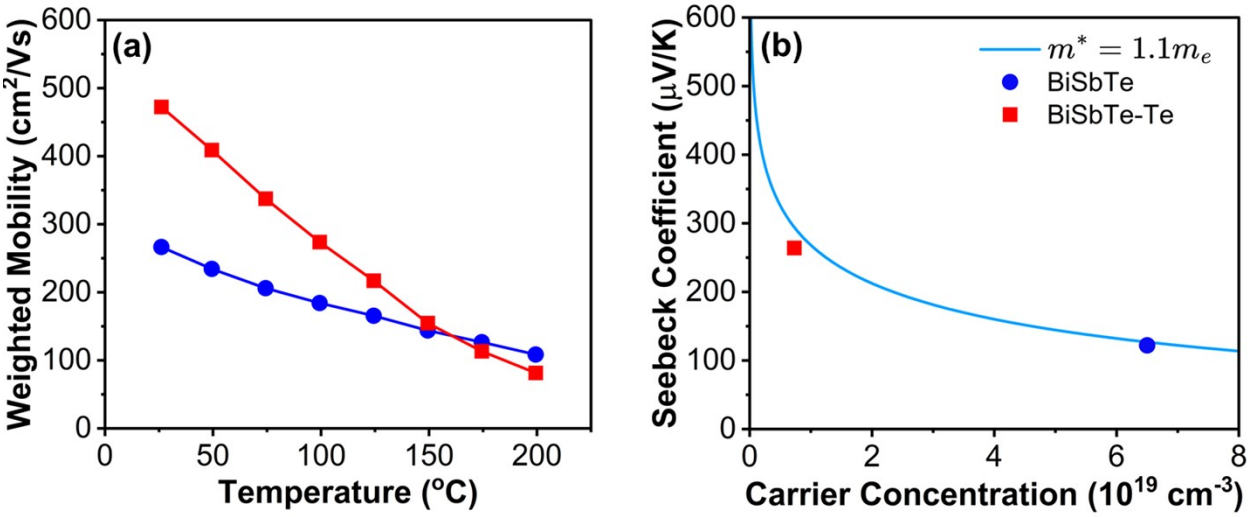

Fig. S10 (a) Weighted mobility of BiSbTe and BiSbTe-Te composites calculated from Seebeck coefficient and electrical conductivity.[4] (b) Pisarenko plot (300K) of Seebeck coefficient vs. carrier concentration using $m^* = 1.1m_e$ found for BiSbTe sample with measured carrier concentration and Seebeck coefficient of BiSbTe and BiSbTe-Te.

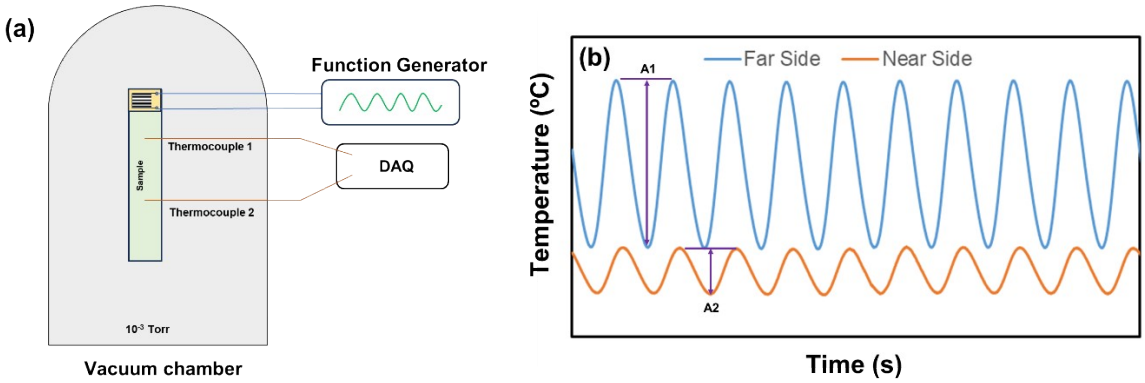

Fig. S11 (a) Thermal diffusivity measurement setup using Angstrom method (b) Sinusoidal temperature vs. time profile for amplitude and phase difference calculation.

The Angstrom method was employed to measure the in-plane thermal diffusivity of the films.[5–10] The versatility of this method is evident in applications ranging from measuring thermal conductivity in thermoelectric films to polymeric nanocomposites and graphene sheets. This method entails the application of a periodic heat source at one end of the film, followed by the detection of temperature wave amplitude and phase at two distinct locations along the sample's length. Precise temperature measurements are facilitated by the deployment of two thermocouples—one positioned near the heat source (near-side) and the other at a more distant location (far side). The chosen frequency range ensures a substantial thermal penetration depth, guaranteeing discernible temperature oscillations at the far-side thermocouple. Under these conditions, the thermal conductivity (k) can be calculated as follows: $\alpha = \frac{L^2}{2dt\ln\frac{A_1}{A_2}}$ (1), $k = \alpha C_P \rho$ (2). Where α is the thermal diffusivity. L, dt, A_1, and A_2 are distance between the two thermocouples, phase difference and amplitudes of the two temperature waveforms. The C_p and ρ are the specific heat capacity and density. The density of the film is measured by measuring the volume and mass of the rectangular sample using a profilometer and a precision balance respectively. The specific heat was taken from a previous work that reported the specific heat of the material of the same composition as this work.[11]

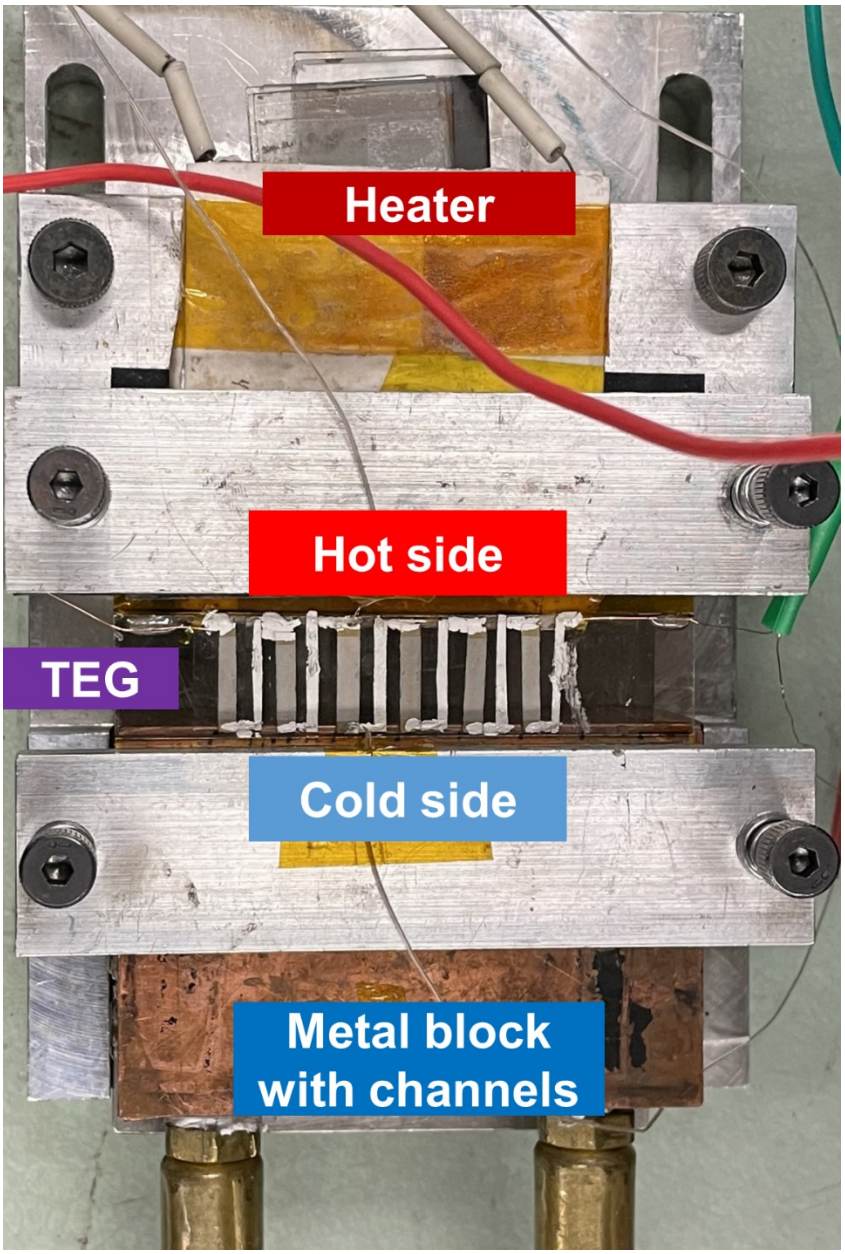

Fig. S12 Thermoelectric device made by p-type BiSbTe-Te legs. The hot and cold sides were controlled by a heater and a metal block with flowing water through it at different site of the device. The temperature on both sides is measured by two thermocouples. TEG device output was connected to a variable load to measure the current varying output power.

Table. S1 Excellent reproducibility of thermoelectric performance of BiSbTe-Te (8 %wt. Te concentration) prepared in different batches.

Sample No	Seebeck Coefficient	Electrical Conductivity	Power Factor

	[μV/K]	[S/cm]	[mW/mK^2]
20220729_S1	264	491	3.42
20220729_S2	259	536	3.60
20220909_S1	262	526	3.61
20220909_S2	263	530	3.67
20220821_S1	252	571	3.64
20220821_S2	262	468	3.21
20220821_S3	263	530	3.67
20220821_S4	262	468	3.21
20221011_S1	261	457	3.11
20221017_S1	258	542	3.61
20221017_S2	260	481	3.25
20221017_S3	263	492	3.40
20221017_S4	257	471	3.12
20221017_S5	260	553	3.74
20230222_S3	259	488	3.28
20230718_S1	264	505	3.52
20230718_S2	255	519	3.38
20230718_S3	269	451	3.26
Average	261	504	3.43
Std. Dev.	3.7	35	0.21

Table. S2 Thermoelectric zT of Bismuth Telluride based p-type materials manufactured by different methods.

Preparation Method	Composition	Room Temperature Figure of Merit, *zT*	Reference

Ink deposition	BiSbTe-Te	1.3	This work
Cyclic Spark Plasma Sintering	BiSbTe-Te	1.4	[13]
Hot Pressing	BiSbTe	1.2	[14]
Screen Printing	BiSbTe_Te	1	[10]
Extrusion Printing	BiSbTe	0.8	[15]
Extrusion Printing	BiSbTe	0.8	[16]
Direct ink writing	BiSbTe	0.5	[17]
Inkjet Printing	BiSbTe	0.1	[18]

References

1 K. Wang, M. Saeidi-Javash, M. Zeng, Z. Liu, Y. Zhang, T. Luo and A. W. Dowling, 2022, pp. 1819–1824.

2 K. Wang and A. W. Dowling, *Curr. Opin. Chem. Eng.*, 2022, **36**, 100728.

3 B. Shahriari, K. Swersky, Z. Wang, R. P. Adams and N. de Freitas, *Proc. IEEE*, 2016, **104**, 148–175.

4 G. J. Snyder, A. H. Snyder, M. Wood, R. Gurunathan, B. H. Snyder and C. Niu, *Adv. Mater.*, 2020, **32**, 1–5.

5 P. G. Bison, S. Marinetti, A. Mazzoldi, E. Grinzato and C. Bressan, *Infrared Phys. Technol.*, 2002, **43**, 127–132.

6 A. J. Angström, *London, Edinburgh, Dublin Philos. Mag. J. Sci.*, 1863, **25**, 130–142.

7 J. M. Belling and J. Unsworth, *Rev. Sci. Instrum.*, 1987, **58**, 997–1002.

8 W. Shang, M. Zeng, A. N. M. Tanvir, K. Wang, M. Saeidi-Javash, A. Dowling, T. Luo and Y. Zhang, *Adv. Mater.*, 2023, **35**, 2212230.

9 M. Saeidi-Javash, K. Wang, M. Zeng, T. Luo, A. W. Dowling and Y. Zhang, *Energy Environ. Sci.*, 2022, **15**, 5093–5104.

10 T. Varghese, C. Dun, N. Kempf, M. Saeidi-Javash, C. Karthik, J. Richardson, C. Hollar, D. Estrada and Y. Zhang, *Adv. Funct. Mater.*, 2020, **30**, 1905796.

11 T. Varghese, C. Dun, N. Kempf, M. Saeidi-Javash, C. Karthik, J. Richardson, C. Hollar, D. Estrada and Y. Zhang, *Adv. Funct. Mater.*, 2020, **30**, 1905796.

12 S. Il Kim, K. H. Lee, H. A. Mun, H. S. Kim, S. W. Hwang, J. W. Roh, D. J. Yang, W. H. Shin, X. S. Li, Y. H. Lee, G. J. Snyder and S. W. Kim, *Science (80-.).*, 2015, **348**, 109–114.

13 H. L. Zhuang, J. Pei, B. Cai, J. Dong, H. Hu, F. H. Sun, Y. Pan, G. J. Snyder and J. F. Li, *Adv. Funct. Mater.*, 2021, **31**, 1–11.

14 B. Poudel, Q. Hao, Y. Ma, Y. Lan, A. Minnich, B. Yu, X. Yan, D. Wang, A. Muto, D. Vashaee, X. Chen, J. Liu, M. S. Dresselhaus, G. Chen and Z. Ren, *Science (80-.).*, 2008, **320**, 634–638.

15 F. Kim, B. Kwon, Y. Eom, J. E. Lee, S. Park, S. Jo, S. H. Park, B. S. Kim, H. J. Im, M. H. Lee, T. S. Min, K. T. Kim, H. G. Chae, W. P. King and J. S. Son, *Nat. Energy*, 2018, **3**, 301–309.

16 F. Kim, S. E. Yang, H. Ju, S. Choo, J. Lee, G. Kim, S. ho Jung, S. Kim, C. Cha, K. T. Kim, S. Ahn, H. G. Chae and J. S. Son, *Nat. Electron.*, 2021, **4**, 579–587.

17 Z. Wang, W. Cui, H. Yuan, X. Kang, Z. Zheng, W. Qiu, Q. Hu, J. Tang and X. Cui, *Mater. Today Energy*, 2023, **31**, 101206.

18 B. Chen, M. Kruse, B. Xu, R. Tutika, W. Zheng, M. D. Bartlett, Y. Wu and J. C. Claussen, *Nanoscale*, 2019, **11**, 5222–5230.